Applied Thermal Engineering 236 (2024) 121477

Contents lists available at ScienceDirect

Applied Thermal Engineering

journal homepage: www.elsevier.com/locate/apthermeng

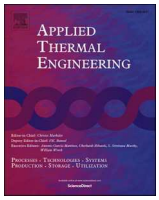

Research Paper

Independent microscale sensing of phase interface and surface temperature during droplet evaporation

Md Tanbin Hasan Mondal [a], Rifat-E-Nur Hossain [a], Ronald Martin [b], Arden L. Moore [a,c,*]

[a] Institute for Micromanufacturing, Louisiana Tech University, Ruston, LA 71272, USA
[b] Electrical Engineering Dept., Louisiana Tech University, Ruston, LA 71272, USA
[c] Mechanical Engineering Dept., Louisiana Tech University, Ruston, LA 71272, USA

ARTICLE INFO

Keywords:
Droplet evaporation
Phase-change heat transfer
Moving contact line
Capacitance sensing
Thermal sensing

ABSTRACT

Despite the important and pervasive nature of evaporative heat transfer phenomena, fundamental questions still remain about the microscopic processes that occur in and around individual droplets on a surface. In order to understand the underlying physics behind evaporative heat transfer, it is critical to have information at the individual droplet level regarding the surface temperature distribution with time as well as the location and speed of the moving multiphase contact line (MCL). In this work, a multifunctional microscale device comprised of a resistance heater, an array of spatially distributed thin-film resistance temperature detectors, and a phase interface sensing capacitance micro-sensor array has been utilized to measure the local heat transfer characteristics and MCL behavior simultaneously for the evaporation of individual sessile water droplets on a horizontal heated surface. The resistance- and capacitance-based operating principles of the micro-device means that it is capable of detecting temperature changes and tracking MCL at the microscale in real time even for applications with limited or no visibility such as within thermal management hardware or processing equipment. Importantly, having knowledge of the MCL's location and speed with microscale precision allows for its influence on surface temperature and heat transfer to be directly studied rather than inferred. Results show that the MCL passage precedes the change in local surface temperature and the duration of the time difference between these events depends on the MCL's speed. In addition, the passage of the MCL accounts for more than 70% of the overall temperature change during the evaporation process.

1. Introduction

Evaporation is an essential phenomenon with ubiquity in everyday life including significant scientific and engineering applications. Studying the heat transfer mechanisms and moving contact line behavior involved in the evaporation of sessile droplets has been a matter of great interest in recent years due to its applicability in diverse fields including medical diagnostics, inkjet printing, DNA mapping, and multiphase thermal management techniques [1–6]. In terms of phase change cooling, droplet evaporation facilitates high heat fluxes due to the significant amount of thermal energy associated with the latent heat of vaporization of the fluid which reduces the thermal resistance between the heat source and sink [1,7].

The thermo-fluid physics of evaporating droplets are comprised of various complex processes, including but not limited to conjugate heat transfer at the moving contact line (MCL) region, the motion of the MCL, micro-convection within the sessile droplet, and surface evaporation [1,3,6]. Indeed, the MCL - a three-phase region where the liquid–vapor interface meets the solid surface - is an area of strong thermal and mass gradients that greatly influences the overall evaporation process. Different physical mechanisms govern the overall dynamics of the evaporation process depending on the experimental environment. When evaporation occurs in an open environment, the diffusive transport of vapor into the atmosphere, the phase transition that occurs at the surface of the droplet, the heat transport within the droplet, and the conduction of heat from the surface to the droplet are among the significant influencing physical processes [8]. Although the physical mechanisms involved in droplet evaporation have been extensively researched, the interdependence of MCL behavior and the associated conjugate heat transfer is not yet comprehensively understood [3,9].

The MCL of a droplet may look like a sharp interface at the macroscale, but actually consists of a combined macro-region and thin-film

* Corresponding author.
E-mail address: amoore@latech.edu (A.L. Moore).

https://doi.org/10.1016/j.applthermaleng.2023.121477
Received 27 March 2023; Received in revised form 6 July 2023; Accepted 1 September 2023
Available online 4 September 2023

micro-region. As Fig. 1 shows, the micro thin-film region comprises an adsorbed film and a transition film, where the adsorbed film results from the strong adhesion interactions between the droplet and the substrate. While the suppression of evaporation in the adsorbed film region is well-established for a liquid droplet in contact with pure vapor, the behavior of the adsorbed film region becomes more complicated in the diffusion-limited evaporation regime such as when the environment is not pure vapor. In this regime, the evaporation rate is limited by the rate at which the vapor molecules can diffuse away from the surface of the liquid into the atmosphere. The disjoining pressure, resulting from the change in relative vapor pressure in the atmosphere, determines the thickness of the adsorbed film region [8,10–12]. The neighboring region of the adsorbed film where the thickness increases is known as the transition film region. This region is home to intense evaporation and very high heat flux values as the liquid–solid adhesion forces are weaker compared to the thin-film region. The transition film thickness varies from 1 to 3 μm [13], much thicker than the adsorbed film but still thin enough to offer only a negligible resistance to heat transfer. The thermal resistance increases with the film thickness in the macro-region consisting of the intrinsic meniscus and micro-convection region. As the increasing film thickness offers growing resistance to the overall heat transfer, both these regions experience lower heat flux values compared to the transition film region. The macro-region holds the droplet's bulk portion and acts as the resource that supplies fluid toward the strongly evaporating micro thin-film regions. The liquid–vapor interface generated from the beginning of the intrinsic meniscus region is what is generally known as the droplet's macroscopic contact angle relative to the substrate's solid surface [3,14,15]. In terms of heat transfer mechanisms, researchers have emphasized the importance of the three-phase contact line in general and the micro-region that contains the transition thin-film in particular as it is this region that possesses the strongest heat transfer characteristics [16,17].

Despite this established viewpoint, unlocking the physical interdependence of the MCL region and local temperature distribution remains a critical need in order to validate models, enable *a priori* surface design, and optimize evaporative cooling processes [17,18]. Numerous approaches in the literature have adopted analytical models that conclude that the transition film between the intrinsic meniscus and non-evaporating adsorbed film regions facilitates the highest evaporative heat fluxes [1,3,5,6,18–22]. Additional works have developed numerical models, including some validated by experimental investigations for evaporating thin liquid films on micro-grooves, which showed up to 80% of the total dissipated heat during droplet evaporation occurs at the transition thin-film region [16,21].

The MCL behavior is the predominant factor that influences the evaporation process of a sessile droplet, and various research works have focused on investigating the substrate's surface properties that significantly affect the MCL behavior and wettability. As an example, in one such work, Sobac and Brutin [23] studied the spontaneous natural evaporation of sessile droplets under atmospheric conditions from nanocoated surfaces of varying wettability with different working fluids. The investigation revealed that the dynamics of the evaporative rate are proportional to the dynamics of the wetting radius, and the greater the contact angle and the more pinned the contact line the shorter the duration of the evaporation process [23]. The heat transfer characteristics at the MCL regions have also been experimentally investigated, although the number of works is relatively limited [16–19,22,24,25]. According to one empirical investigation with hydrofluoroether engineered fluid (HFE), the local heat fluxes at the contact line region could be 5.4–6.5 times greater than the average heat flux at other regions of the evaporating droplet [18]. Experiments with other nonaqueous liquids such as heptane have demonstrated that a 50 μm sub-region between the intrinsic meniscus and adsorbed film region facilitates 45–70% of the total heat transfer throughout the evaporation process [16,17]. Additional experimental investigations with HFE for bidirectional movements of its MCL observed higher heat fluxes at the three-phase contact line region for advancing movement compared to the receding motion of the moving interface [18,25]. The advancing MCL causes a significant increase in the temperature change rate per unit length by deforming the thermal boundary layer between the fluid and heated wall, which in turn enables a high heat transfer rate [24]. These experimental approaches have also demonstrated that during the advancing movement of MCL, the evaporative heat fluxes near the moving three-phase interface increase with the increasing speed of the MCL. Interestingly, in contrast the highest heat fluxes near this region during receding movement are independent of the speed of the MCL [18,25]. Clearly, the MCL speed and direction are important factors in controlling the rate of heat transfer in this critical region.

Measuring the local temperature distribution and correlating it with the MCL behavior for an evaporating droplet has proven to be challenging due to the requirement of using non-intrusive microscale and transient measurement techniques [16]. Experimental approaches within the literature like those cited above have adopted macroscopic thermocouple probes, which present significant constraints in terms of temperature resolution, response time, and potential invasiveness to the droplet under study [1,26]. To overcome low spatial resolution with macroscopic sensing techniques, some researchers have utilized thermochromic liquid crystals (TCLs), organic compounds with an optically active twisted molecular structure that changes color with temperature change within a specific range. Researchers studied the evaporation of volatile liquid droplets deposited on a heated substrate in a pure saturated vapor environment via TCLs, where the TCLs reflected a distinct color depending on the temperature, and a charge-coupled device (CCD) camera captured the color information for image processing to convert it into temperature readings [27]. Although TCLs offer certain advantages over macroscopic probe techniques, measurement uncertainty and low shelf-life of the crystals limit their broader applicability [1,16,17].

Infrared (IR) thermography has become a popular choice for measuring local temperature distribution because of its non-contact nature, higher spatial resolution than thermocouples, and good temperature sensitivity. Although IR thermography is a well-established technique, it can only be employed to measure temperature distribution if optical access to the surface is available in the wavelengths of interest [28]. Moreover, the limitation on the camera resolution and

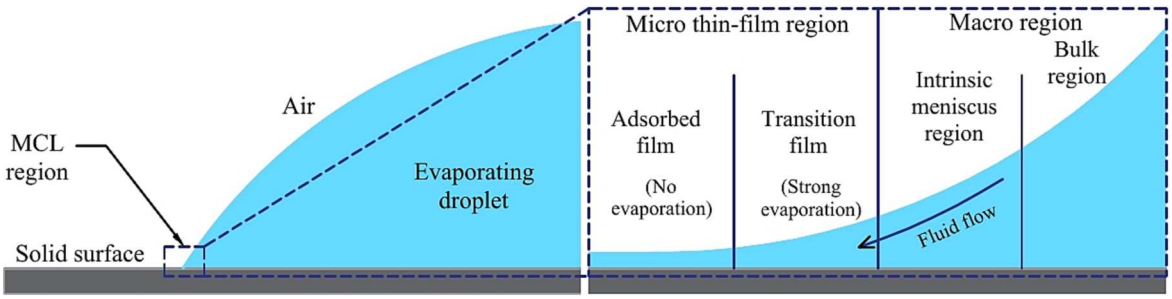

Fig. 1. Schematic of the contact line region of a hydrophilic evaporating droplet on a solid surface.

wavelength diffraction limit often restrains IR thermography from precise quantitative detection of the temperature distribution at the thin-film region [1,16,17]. Microfabricated temperature sensors are attractive for microscale temperature sensing of evaporating droplets because of their high temporal and spatial resolution [29] so long as they are implemented in a non-intrusive manner to the droplet under study. A few fundamental works exploring local processes in pool boiling have developed specialized micro-thermocouples as these are smaller and faster, whereas the macroscopic temperature probes lack sufficient accuracy regarding spatial and temporal dimensions. Measurements of local heat transfer mechanisms in dynamic heat transfer processes require thermal sensors with sufficient fast response; these microfabricated thermocouples facilitated the effective investigation of local temperature fluctuations and spatial wetting dynamics for phase change heat transfer processes [30–32]. Similarly, several significant experimental investigations of heat transfer distributions at the interface between a solid substrate and fluid have employed microscale resistance heater arrays on a quartz substrate. These approaches incorporated infrared cameras with high-speed CCD imaging and revealed the significance of specific heat transfer mechanisms in addition to microlayer evaporation for boiling processes [33–36]. An experimental investigation measuring interfacial temperature distribution during droplet evaporation of ethanol on a copper substrate also coupled infrared thermography with a CCD camera [37]. Another experimental approach with a novel technique of measuring heat transfer parameters utilized infrared thermometry to investigate wall temperature and heat flux distribution during droplet evaporation of PF-5060. According to this work, as the droplet diameter decreased due to evaporation the highest heat flux values occurred at the receding moving contact line of the droplet [28]. Other fundamental works on the experimental investigation of phase change heat transfer have developed and implemented novel test rigs for inspecting boiling heat transfer from a hot plate to planar and impinging jets. These works employed a micro-optical technique with a probe diameter of approximately 1.5 μm for efficient tracking of droplet diameter or dry spot size of microscale droplets or bubbles [38,39]. These micro-optical probe works investigated several nucleate boiling experiments under steady-state and transient conditions for different wetting fluids such as FC-72, isopropanol, and water [40].

However, for all these methods knowledge of the surface temperature distribution alone does not necessarily provide the strong, direct experimental link to microscale MCL dynamics needed to advance the field and overcome its commonly invoked assumptions in regard to interdependence. Besides temperature, a comprehensive understanding of the physical mechanisms involved in droplet evaporation requires correlation of MCL location and speed with the local temperature distribution. Several seminal works within the literature emphasized photographic inspections of droplet structures during the evaporation process and implemented very complex techniques due to continuous capturing schemes still underdoing development during that period. The implementation of the flash photographic method provided significant insights for various phase change heat transfer processes, including but not limited to Leidenfrost evaporation, collision dynamics of a liquid droplet on a hot surface, and nucleate boiling [41–43]. Photographic inspection also played a decisive role in the fundamental work on the investigation of contact angle temperature dependence of water droplets as the contact angle measurements were obtained from the captured photographs of the droplets [44]. High-speed photographic techniques and heat transfer measurements played equally significant roles in another pivotal work investigating the effects of surface roughness on water droplet evaporation [45]. Recent experimental approaches within the literature have employed high-speed cameras and optical image processing techniques to document MCL movement during evaporation of small-scale droplets but are limited due to their macroscopic spatial resolution and visibility, i.e. line of sight and viewing angle [46–49]. As an alternative, electrical sensing approaches may facilitate real-time tracking of MCL location at the microscale and without necessarily requiring line-of-sight visibility or set viewing angles [46,48,50].

This work experimentally reveals the physical interdependence of MCL motion and local temperature distribution underneath an evaporating droplet via a novel combined microscale sensing approach. The experiments reported in this work utilized a custom-designed microelectromechanical (MEMS) device comprised of spatially distributed thin-film resistance temperature detectors (RTDs) and an array of interdigitated electrode (IDE) capacitance-based phase interface sensors for investigating the heat transfer phenomena and MCL motion for evaporating droplets on the microscale. This novel approach of combining a capacitance-based phase interface sensing scheme with temperature-sensing microfabricated RTDs allows for simultaneous and independent sensing of both critical aspects with high spatial and temporal resolution. Results of this work show that the passage of the MCL precedes the actual change in local surface temperature and the duration of time lag between these two events depends on the speed of the MCL. In addition, it is shown that the MCL speed depends on the surface temperature. Specifically, higher surface temperature facilities higher MCL speed, which in turn causes greater differences in wall temperature underneath the liquid bulk and dry region, consequently enabling higher heat flux values. Further, the three-phase contact line region of an evaporating water droplet contributes more than 70% of the overall temperature change during the evaporation process.

2. Methodology

A. Micro-device overview

The experimental investigations reported in this work have employed a multi-functional MEMS device comprised of a thin-film resistance heater, a series of RTDs, and an array of phase interface-tracking IDE capacitance micro-sensors. Fig. 2(a)-(c) show laser microscope images of the micro-device used for studying droplet evaporation. Fig. 2(d) shows a diagram of the cross-sectional view of the micro-device, where the resistance heater resides directly on top of the starting soda-lime substrate. The first of the three polyimide polymer layers resides between the resistance heater and the RTDs to provide electrical insulation. A series of 28 platinum thin-film RTDs are spatially oriented from the center of the device atop the first polymer layer to measure the local temperature distribution beneath the evaporating droplets at various locations. Fig. 2(a) shows a detailed view of the sensing zone. For both the RTDs and IDEs, we follow a numbering scheme where 1 corresponds to a sensor closest to the center and numbering increases with radial distance towards the periphery of the sensing zone. Naming is further accomplished with an L for a sensor to the left of the device center and R for a sensor to the right. Hence, RTD-1R is the RTD closest to the device center on the right while RTD-14L would be the farthest RTD to the left of the device center. A similar scheme is used for the capacitance sensors, i.e., CS-1R, CS-3L, etc. It should be noted, however, that despite centering the droplet on the device at the start of an experiment, evaporation does not necessarily occur symmetrically or end exactly at the device center.

An RTD works based on the operating principle that the electrical resistance of metals having a positive temperature coefficient of electrical resistance changes linearly with temperature. Since the temperature sensing depends on the element resistance, any added resistance from the lead wires, contacts, or connectors will result in measurement error for an RTD [51,52]. As shown in Fig. 2(c), a four-probe style of RTD was utilized in this project that eliminates the influence of contact and lead resistances and allows the resistance of the actual temperature-sensing central four-probe region of each RTD to be accurately known. The spatial resolution of the temperature sensing scheme employed in this work is 40 μm as dictated by the spatial separation between each consecutive RTDs.

The capacitance-based phase interface IDE micro-sensor array was

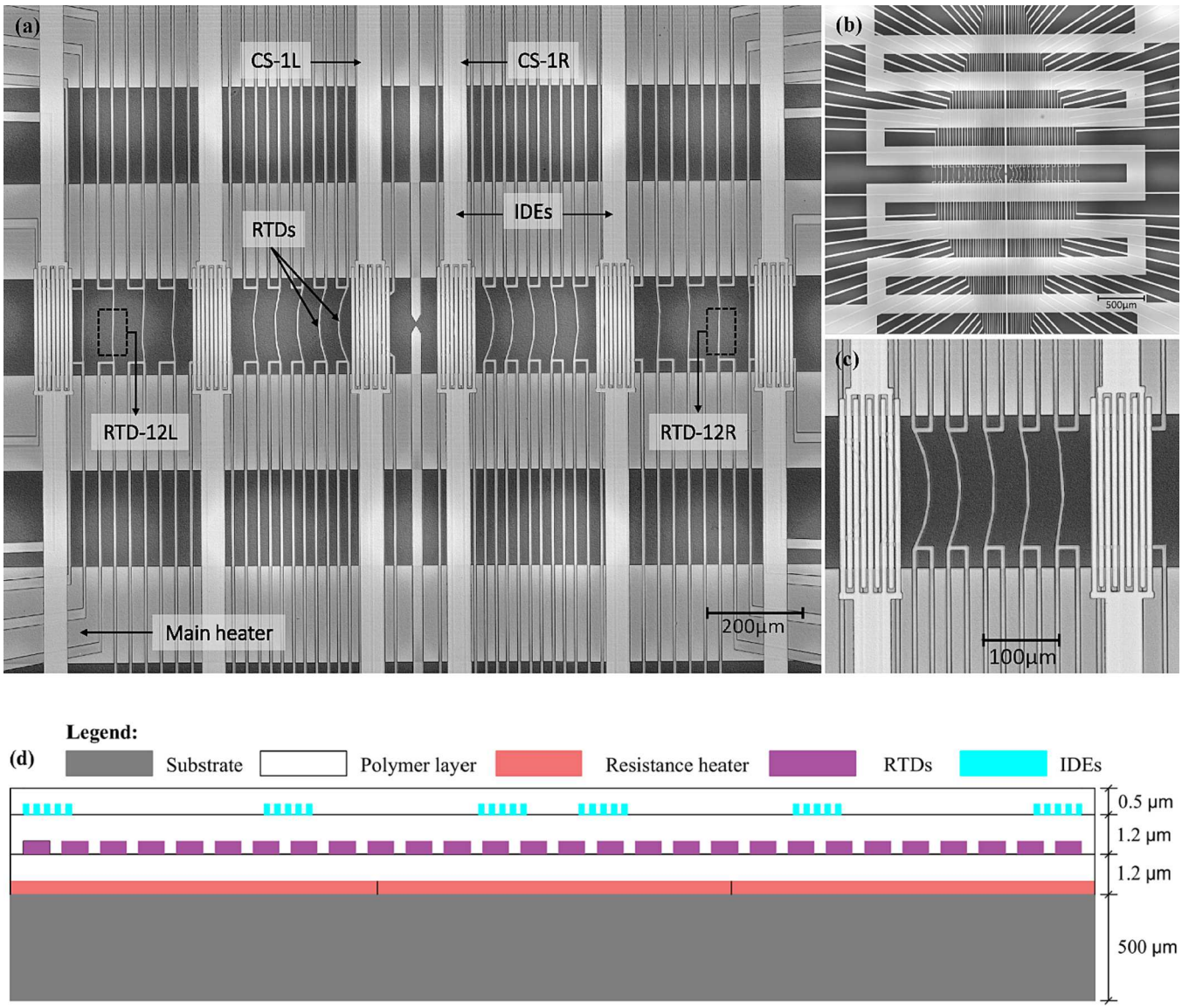

Fig. 2. Laser microscope images of the micro-device. (a) A detail of the sensing zone containing six IDE capacitance micro-sensors, a series of four-probe type RTDs, and a resistance heater. (b) Thin-film resistance heater (serpentine feature) located beneath RTD and IDE layers. (c) A close-up of the sensing region showing detailed view of the IDEs and RTDs. (d) Schematic diagram of the cross-section of the micro-device. Conceptual image, not to scale.

fabricated on top of the second polymer layer for microscale tracking of the moving contact line behavior during the evaporation process. In our prior works, the IDE-based sensing scheme demonstrated effectiveness for microscale tracking of the MCL for advancing and receding aspirated water droplets as well as during droplet evaporation processes [48,53]. The capacitance micro-sensor works based on the operating principle that the relative permittivity of the region above the interdigitated electrodes changes with the passage of the MCL of the droplet, which in turn causes a detectable change in capacitance in the sensor array [46,48,49,53]. This device employed a thin (500 nm) insulating layer of polyimide directly atop the microfabricated IDEs, which possesses relative permittivity ε_r of 3.4 [54]. With the dosing of the water (ε_r= 80) [49] droplet, the capacitance micro-sensors experience a significant change in relative permittivity in the sensed region compared to when mostly air (ε_r = 1) [48] occupies the area directly on top of the IDEs. The IDE array represents this change in relative permittivity by exhibiting a change in capacitance signal output, which denotes the location and passage of the MCL during the experiment. Further details on this sensing scheme including its implementation and validation can be found in our previous works [48,53].

B. Microfabrication process

A 500 μm thick soda-lime glass wafer was chosen as the starting substrate for this micro-device because of its low thermal conductivity, microfabrication compatibility, and ability to enhance the strength of the capacitance signals while reducing coupling effects for multiple IDE sensors in adjacent proximity. The microfabrication of the MEMS device consists of the deposition of platinum (Pt) as the resistance heater, RTDs, and capacitance micro-sensor array by standard photolithography and lift-off techniques. The microfabrication process also includes the spin coating of the thin insulating polyimide polymer layers to provide electrical insulation between metal layers and to enable a thin topmost protective coating. To begin, a 100 nm thin film of Pt was patterned as the serpentine resistance heater directly on top of the starting substrate (Fig. 2(b)), where a 15 nm thin film of titanium (Ti) acted as the adhesive layer. The deposition of the Pt layer was carried out in an AJA ATC sputtering system with a commercially available 3-inch sputtering target, which provided a deposition rate of 75–100 nm/min at 200 W. This same Pt deposition process was used in turn for all three metallic layers, i.e., the main heater, RTD, and IDE layers.

A spin-on polyimide (PI-2611) was commercially obtained from HD Microsystems for depositing the insulating layers. The stock PI-2611 polymer provided a comparatively thick layer of 2.8 μm at a spin speed of 5000 RPM. Adding N-Methyl-2-Pyrrolidone (NMP) with PI-2611 provides thinner layers at the same spin speed. A diluted PI-2611 (75% PI-2611 + 25% NMP) provided a thin film of 1.2 μm atop the resistance heater, which acted as the electrically insulating layer between the resistance heater and the RTDs. Next, the array of 28 RTDs was patterned on top of the initial polyimide insulation layer. A second 1.2 μm polyimide film was then deposited via spin coating to serve as the electrical insulation between RTDs and the capacitance-sensing IDE micro-sensors to follow. The IDEs utilize a 70 nm thin layer of Pt deposited on top of the second insulation layer of polyimide and are shown in Fig. 2(a). Finally, a thin layer (~500 nm) of polyimide was deposited on top of the IDEs to create a topmost protective coating of the micro-device and prevent shorting when a water droplet is present. Bond pads for every sensor on each deposited metal layer were located at the chip periphery on the starting substrate for convenient and reliable wire bonding. After deposition of the final polymer layer, the three polyimide layers were patterned via reactive ion etching with an etchant of 5 sccm CF_4 and 20 sccm of O_2 to remove unwanted polymer from the edges of the chip before depositing the bond pads onto the exposed soda-lime surface.

C. Experimental setup

Fig. 3 shows a schematic of the experimental setup for studying the droplet evaporation process along with the micro-device to be tested. The bond pads of the microfabricated test device were individually wire-bonded with bond pads of a commercially obtained leaded ceramic chip carrier (Spectrum Semiconductor Materials Inc.). The test device and ceramic chip carrier assembly was connected with a pin grid array (PGA) zero insertion force socket, which was in turn embedded onto a custom sample stage. This assembly was aligned underneath the syringe of a computer-controlled drop shape analyzer (DSA 25E, KRÜSS Scientific) for the evaporating droplet studies as illustrated in Fig. 3. During experiments, the dosed volume of the water droplets was 6.0 μL with a dosing rate of 1.0 μL/s. The initial temperature of the droplet was 24.0 °C.

The DSA provided controlled dosing of individual water droplets and an optical camera attached to the DSA recorded the evaporation process during each experiment. The images and videos captured by the DSA during the evaporation process like those shown in Fig. 4 enabled the validation of the intended functionality of the micro-device. A DC power supply provided the necessary power to the resistance heater to control the droplet's evaporation by facilitating elevated surface temperatures

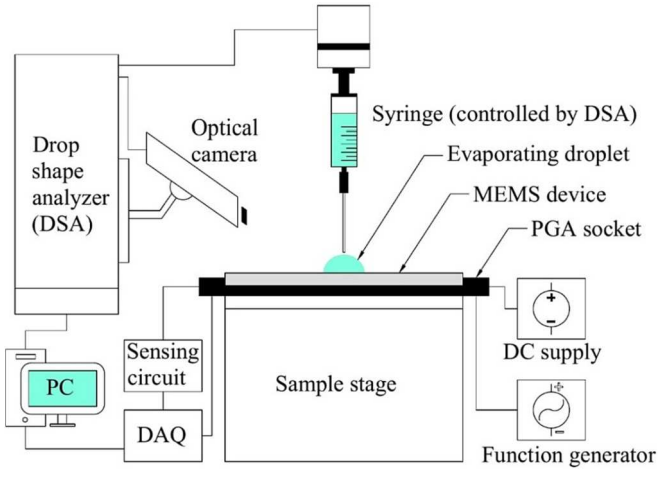

Fig. 3. Schematic of the experimental setup. Conceptual image, not to scale.

during the experiment. As Fig. 4 depicts, the DSA facilitated precise dosing of a water droplet through a needle with a diameter of 0.50 mm in the approximate center of the microdevice. The droplet entirely covered the sensing zone of the microdevice, which allowed for simultaneous measurement of temperature distribution and the tracking of the MCL's speed and location. The collage images presented in Fig. 4 illustrate the changes in volume and contact angle of the droplet due to evaporation from the heated polyimide surface of the microdevice. The DSA recorded the changes in volume, diameter, and contact angle as the evaporation progressed for all the experiments conducted in this study. Further details regarding DSA-tracked contact angle and droplet volume data can be found in the Supplementary Materials section. To prevent self-heating of the RTDs, a small current of 0.2 mA was supplied from a separate DC supply to the power leads of each RTD employed during the experiment. The voltage leads of each RTD, and capacitance micro-sensor were connected to a computer-controlled multichannel data acquisition (DAQ) system (NI 6255, NI).

Separate from the evaporation experiments, an IR camera (A300, FLIR) and a commercially available macroscopic thermocouple (Type J, Omega) were employed to calibrate the relationship between top surface temperature and power input from the DC supply. During the calibration, the thermocouple was placed on the microdevice's sensing zone, ensuring good thermal contact. The IR camera continuously monitored the temperature changes of the polyimide surface simultaneously with the thermocouple for different power inputs. Before the calibration, a standard temperature humidity meter (Fluke 971) facilitated proper adjustments of the IR camera's emissivity parameters and the thermocouple's temperature reading. The calibration of the surface temperature was carried out in the temperature range from 35 °C to 80 °C. The power inputs (ranging from 124.5 mW to 612.7 mW) were calculated from the supplied DC voltage and the current input employed to the resistance heater.

The passage of the MCL and the local temperature distribution underneath an evaporating droplet were measured at three different surface temperatures by employing the micro-device shown in Fig. 2. Surface temperatures ranging from 53.0 °C to 69.7 °C were attained by applying known power inputs from the DC supply to the resistance heater of the micro-device. For the greatest power input of 612.7 mW, the maximum temperature difference between the micro-device's top surface and temperature sensing RTD layer was found to be 0.04 °C, which is negligible compared to the magnitude of the temperature changes observed during these experiments as well as all others conducted at all lower heater powers. As such, we present the RTD-reported temperatures as being representative of the surface temperature within experimental uncertainty. The calculation of temperature difference between the top surface and the RTD layer can be found in the Supplementary Materials. Each of the twelve RTDs employed for the experiments exhibited a change in voltage outputs with the temperature change of the microdevice's top polyimide surface. The recorded output voltages of each RTD were converted into resistance values by employing the known current input of 0.2 mA. Each temperature step from the resistance heater calibration and actual experiments provided an average resistance value for the RTDs, which yielded a linear regression relationship between temperature and resistance. This linear regression relation provided temperature outputs corresponding to the resistance changes in the RTD arrays throughout the evaporation process. More details on the surface temperature and RTD calibration are in the Supplementary Materials section. An analysis of measurement uncertainty showed that the RTD temperature sensing scheme could be employed in its current implementation to measure local temperature with a precision of ± 0.2 °C based upon signal-to-noise ratio. An absolute accuracy of ± 1.2 °C was determined for the RTDs due to calibration against thermocouples or the IR camera, each of which have their own limits of accuracy. It is important to note, however, that the vast majority of this absolute uncertainty is expected to be bias error rather than random error such that measurements of temperature differences by

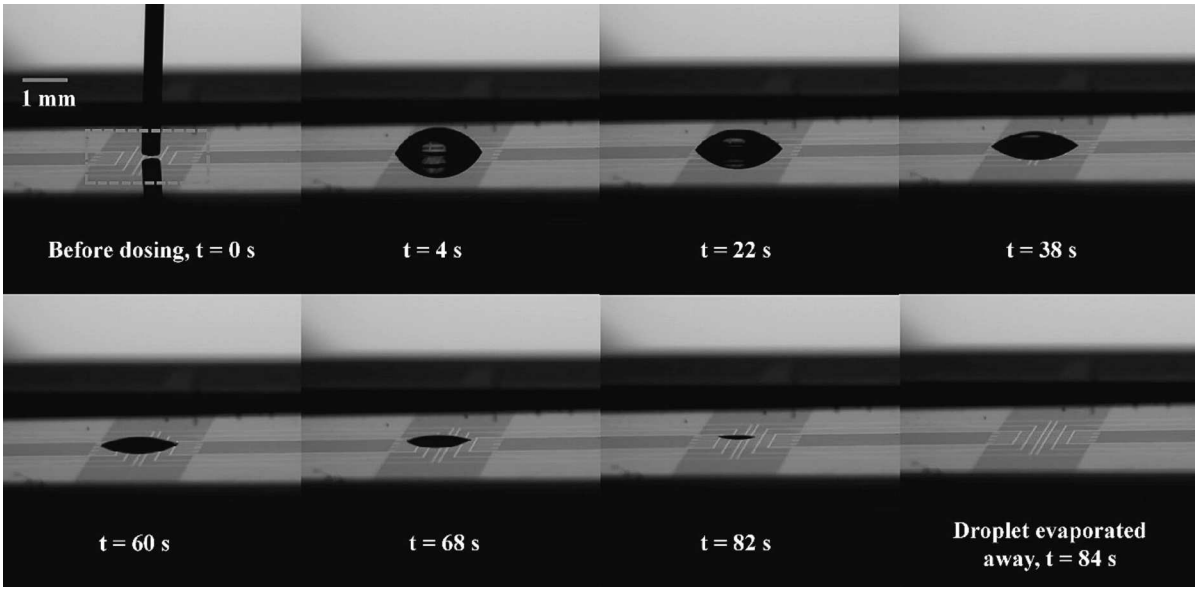

Fig. 4. Representative optical image composite from the DSA for an evaporating droplet during an experiment. The dashed box at the top left of the collaged image highlights the sensing zone of the micro-device.

RTDs calibrated against the same standard can still have smaller uncertainty conservatively estimated at ± 0.5 °C. A propagated relative error of 11% was determined for lateral heat flux values of the evaporating droplet. The details on this measurement uncertainty analysis can be found in the Supplementary Materials.

3. Results and discussion

Fig. 5 gives representative results of absolute capacitance change (%) and surface temperature response for the evaporation process of a 6 μL water droplet at a surface temperature of 69.7 °C from the initial dry state and through the subsequent droplet dosing and evaporation. As Fig. 4 shows, the dosing of the water droplet on the heated polyimide surface of the microdevice was carried out via a needle attached to the syringe controlled by the DSA. Before dosing, the syringe's needle with a diameter of 0.50 mm was manually placed above the center of the microdevice. Water droplets of 6 μL in volume sufficiently covered the sensing zone of the microdevice, which was 1.5 mm in length from the leftmost to the rightmost RTD/IDE, and DSA provided controlled dosing of the same volume of water droplets for all experiments at varying surface temperatures. Since the dosing of water droplets did not facilitate precise alignment of the droplet's center with the microdevice's center or corrections after dosing, the droplets in this experiment evaporated in an asymmetric manner with respect to the exact center of the microdevice, with the MCL crossing the sensing region from right to left with respect to Fig. 2. The droplets were observed to evaporate symmetrically with respect to their own center, however.

As Fig. 5(a) shows, with the dosing of the water droplet, the six capacitance micro-sensors exhibited a simultaneous rise in capacitance signal and retained it until the MCL passed through the sensor region near the end of the evaporation process. The capacitance-based micro-sensors also demonstrated sequential time lag between one another, which facilitated a precise tracking of the speed and location of MCL as the droplet evaporated. This is difficult to discern from the full time-scale data in Fig. 5(a) but will be apparent in subsequent figures that focus on time windows specific to the MCL passage. Fig. 5(b) shows the temperature values detected by the twelve functioning RTDs on the micro-device. At the beginning of the experiment, the RTD signals report room temperature until the DC supply powered the resistance heater of the micro-device to reach the desired surface temperature. With the dosing of the water droplet, the RTDs detected a sudden decrease in surface temperature and an eventual return to previous temperature readings as the droplet evaporated. The change in surface temperature throughout the evaporation process detected by the RTDs correlates in time to the changes in capacitance signals referring to the MCL passage, which validates the dual functionality of this micro-device. Additional figures in Supplementary Materials similarly portray the capacitance change and temperature with time over the entire experiment for an evaporating droplet of the same volume (6 μL) at surface temperatures of 61.0 °C and 53.0 °C, respectively, where the overall evaporation process was completed over longer time periods compared to the experiment conducted at the surface temperature of 69.7 °C. It is important to note that both the RTDs and IDEs were labeled according to a specific naming convention in our experiments. This convention assigns a value of 1 to the sensor closest to the center, with subsequent sensors numbered in increasing order as their radial distance moves toward the periphery of the sensing zone. Additionally, we utilized an "L" designation for sensors located to the left of the device center and an "R" designation for sensors situated to the right. As the annotated examples in Fig. 2 depict, CS-1L represents the IDE nearest to the device center on the left side, while CS-3L indicates the IDE located furthest to the left from the device center. A similar naming scheme was employed for the RTDs, such as RTD-1R, RTD-13R, RTD-2L, RTD-14L, etc.

Since all the experiments reported in this manuscript took place in an open environment, we investigated the effect of large-scale convective flow or air currents on the RTDs or IDEs employed to measure the temperature distribution and track the MCL. As shown in Fig. 5, the IDE signals did not depict any noticeable fluctuations above signal noise levels before the droplet dosing or after the evaporation cycle when the sensing region is bare to the open environment. Similarly, the measured temperature readings via the RTDs during these time periods also did not exhibit any fluctuations above signal noise levels that abrupt air currents would be expected to cause. For both sensor types, signal changes caused by the evaporation process were significantly larger than noise levels prior to and after droplet presence, indicating that the effect of air currents or large-scale convective flow were negligible in comparison. Further, attempts to quantify air current movement in the vicinity of the setup with an anemometer produced no readings as any movement was below the instrument's lower threshold.

As the temperature distribution plot in Fig. 5 portrays, during the dosing of the water droplet where the MCL is advancing over the sensing region the RTDs exhibited a greater temperature change compared to

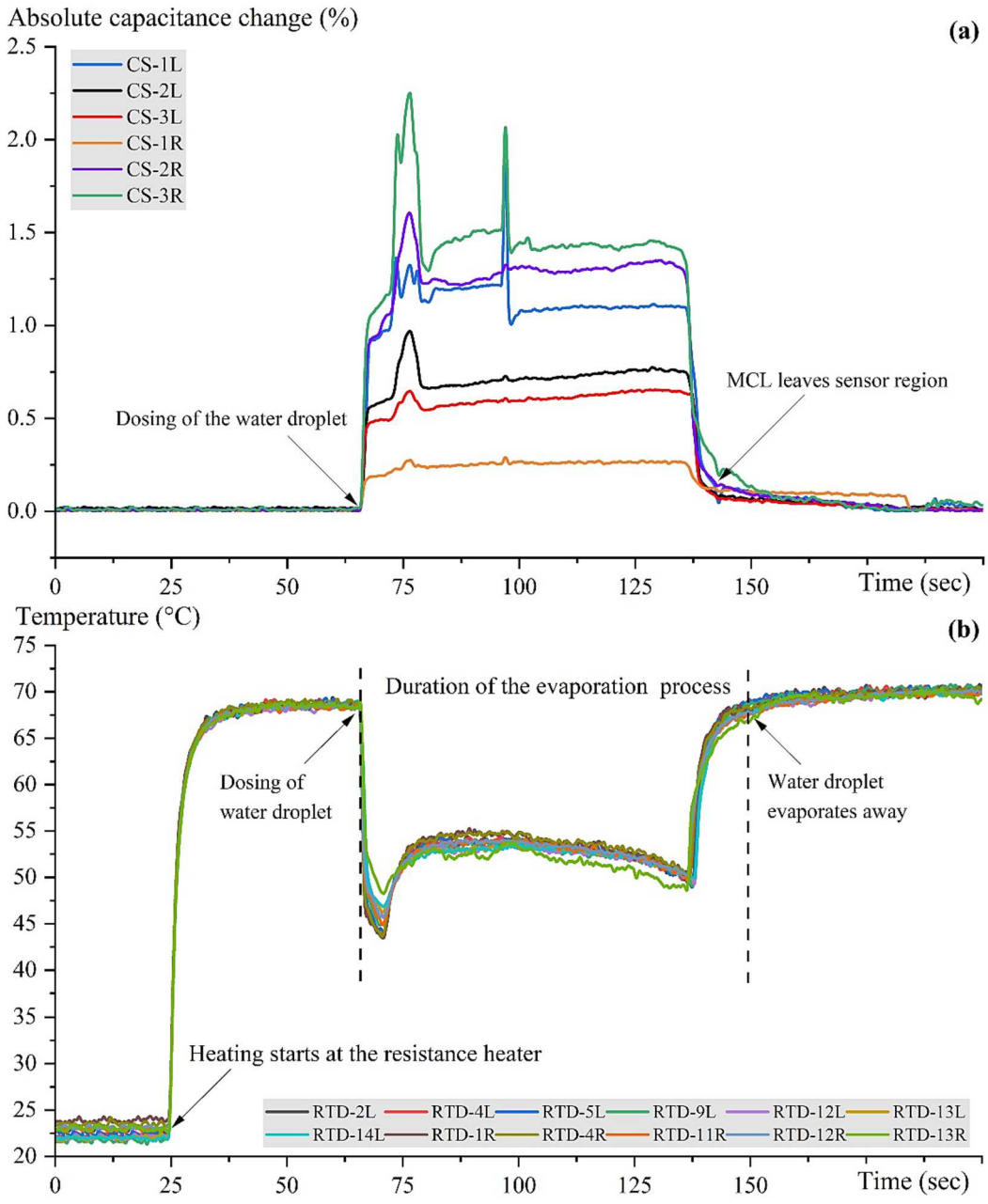

Fig. 5. Evaporation process of a 6 μL water droplet on a heated polyimide surface at 69.7 °C (a) absolute capacitance changes with time using six capacitance micro-sensors (CS-1 to CS-6), (b) temperature distribution with time employing twelve functioning RTDs.

the temperature change associated with a receding MCL at the end of the evaporation process. For example, during the experiment performed at a surface temperature of 69.7 °C, the advancing MCL caused an average temperature drop of 22.5 °C whereas the receding MCL near the end of the evaporation process produced a temperature rise of 19 °C. Similarly, the average temperature change caused by the advancing movement of MCL was, on average, 5.6 °C and 6.1 °C higher compared to the temperature changes caused by receding MCL near the end of the evaporation process for experiments performed at surface temperatures of 61.0 °C and 53.0 °C, respectively. As summarized in Table 1, these results show a non-negligible difference in temperature change caused by advancing and receding movement of MCL, and the magnitude of temperature difference depends on the surface temperature-dictated MCL speed. Further, the greater temperature change for an advancing

Table 1
Summary of MCL passage, speed, and its effects on the thermal response for droplet evaporation.

Surface temperature	Advancing MCL speed**	Temperature change by advancing MCL	Receding MCL speed**	Temperature change by receding MCL	Time lag between MCL passage and thermal response
69.7 °C	1.31 mm/s	22.5 °C	0.95 mm/s	19.0 °C	0.81 s
61.0 °C	1.28 mm/s	19.8 °C	0.51 mm/s	14.2 °C	1.27 s
53.0 °C	1.29 mm/s	15.6 °C	0.47 mm/s	9.5 °C	1.43 s

** The propagated total uncertainty for MCL speed values is +/- 0.12 mm/s.

MCL with comparable speed to a receding MCL is found to be greater, which is in agreement with existing studies [18,25] and is attributable to deformation of the thermal boundary layer between the fluid and heated surface [24].

By focusing in on shorter time windows associated with MCL passage, the combined temperature and MCL tracking data can be utilized to measure the sequence and timing of MCL passage and thermal response events relative to one another. The local temperature distributions for experiments conducted at surface temperatures of 69.7 °C and 61.0 °C shown in Figs. 6 and 7 (left axes) demonstrate that when the water droplet evaporated away and the MCL was receding, the RTD on the right was first to detect the temperature changes associated with the passage of the MCL. These figures also exhibit sequential time lag among the RTDs, where the leftmost RTD was last to detect the temperature changes. The capacitance-based micro-sensors portrayed similar sequential capacitance changes referring to the passage of the MCL. As also shown in Figs. 6 and 7 (right axes), the rightmost capacitance sensor CS-3R first detected the course of the MCL, whereas the capacitance-sensor CS-3L spatially located at the leftmost side was the last to report a change in capacitance signal. The collaged images captured via the DSA (Fig. 4) demonstrated that the droplet's volume gradually reduced from the right to the left side of the device (relative to the center) due to the evaporation process, which provides a practical agreement with the data obtained from the micro-device. However, due to the unconstrained nature of the evaporation process, the passage of the MCL did not always follow this behavior for each experiment. The temperature distribution and capacitance change plots in Fig. 8 depict a separate experiment where the water droplet first evaporated away from RTD-14L and RTD-6R was the last sensor to detect the temperature change, i.e., the movement of the MCL was in the opposite direction relative to the naming convention. Regardless of direction, however, the tracked path of the MCL by the capacitance sensor array was identical to the response sequence reported by the RTDs, which validated the versatile functionality of this micro-device regardless of the direction of motion of the MCL.

Figs. 6-8 show that regardless of the surface temperature, the capacitance sensor array reports MCL passage *before* temperature changes. The droplet evaporation study at 69.7 °C shows that capacitance-sensor CS-3L detected the transition of the MCL at 137.13 s, whereas the spatially equivalent temperature sensor RTD-14L detected the temperature change associated with this transition 0.81 s later. Similarly, experimental results at 61.0 °C show that capacitance-sensor CS-3L indicated a sudden fall in capacitance signal at 166.48 s, while it took 1.27 s longer for the corresponding RTD to demonstrate a change in temperature. While it has been previously known that the MCL serves as a region for significant heat transfer, these results show that the MCL passage precedes the actual change in local surface temperature and that the duration of time between these events depends on the speed of the MCL as summarized in Table 1. For example, the speed of the receding MCL near the end of the evaporation process for the experiment performed at 69.7 °C was 0.95 mm/s, which facilitated a shorter time lag between MCL passage and associated thermal response. Conversely, the investigations conducted at 61.0 °C and 53.0 °C with slower speeds of receding MCL gave longer time lags between these two events. Table 1 reports only the time lags for the receding MCL movement associated with undisrupted evaporation, whereas the advancing MCL associated with droplet dosing is considered a more artificial event required to begin the experiment under controlled and repeatable conditions.

We conducted a thorough analysis to determine the thermal time constant of an individual RTD. This was done to ensure that the observed time delay between the passage of MCL and the thermal response was not influenced by response lag in the RTDs. Our analysis considered the dimensions of the RTDs, the lower bound heat transfer coefficient for an evaporating sessile droplet, and the thermophysical properties of platinum. We also took into account the contribution of the four lead wires of the RTDs. The results of our analysis showed that the thermal time constant of the RTDs was in the range of 0.5–1 ms, which is to be expected given the microscope size of the individual RTDs. Microfabricated temperature sensors have a rapid thermal response, which is one of their key advantages over macroscopic ones. After comparing our results to the observed time lag values presented in Table 1, which are on the order of 1–2 s, we conclude that the speed of MCL propagation predominantly determines the time delay observed in the thermal response. The effect of response lag caused by resistance in the RTDs is negligible. It is important to note that the presence of surface contaminants can potentially affect the MCL's propagation speed on the microdevice's top polyimide surface. To prevent this interference, we gently cleaned the sensing zone of the microdevice after each

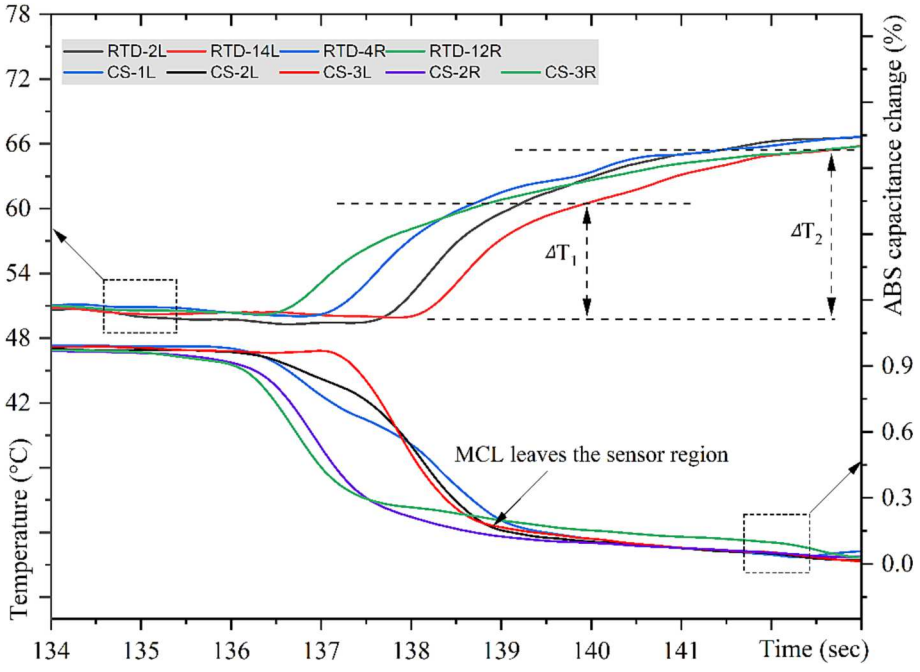

Fig. 6. Local temperature distribution and change in capacitance signal on the outset of droplet evaporating away from the heated polyimide surface at 69.7 °C.

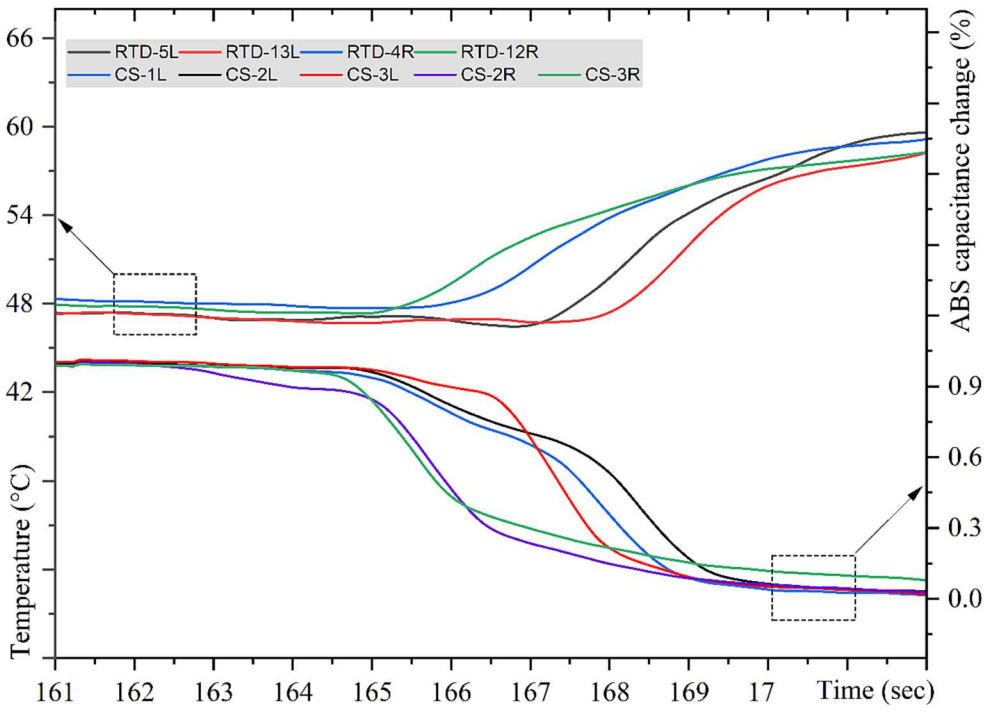

Fig. 7. Local temperature distribution and change in capacitance signal on the outset of droplet evaporating away from the heated polyimide surface at 61.0 °C.

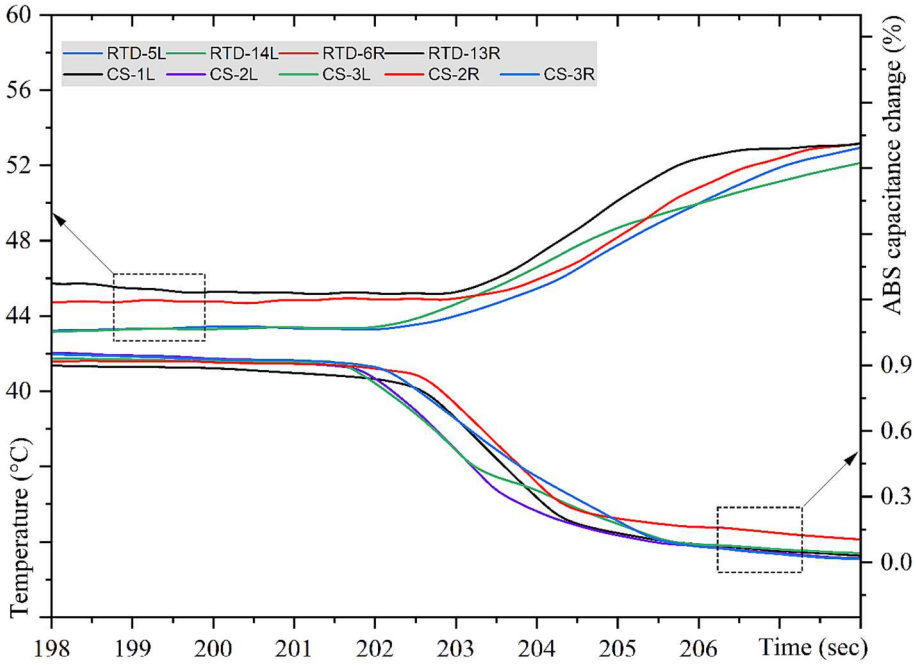

Fig. 8. Local temperature distribution and change in capacitance signal on the outset of droplet evaporating away from the heated polyimide surface at 53.0 °C.

experiment using cleanroom swabs soaked in acetone, isopropanol, and deionized water.

As the capacitance sensor CS-3L demonstrated in Fig. 6, the MCL of the evaporating droplet moved away from the sensor region at 138.96 s. Since the passage of the MCL preceded the actual change in local surface temperature and the time lag between these two events was 0.81 s; therefore 139.77 s revealed the exact temperature change associated with the MCL passage. In this evaporation process, the change in temperature due to MCL passage, denoted by ΔT_1, was 9.7 °C, and the overall temperature change (ΔT_2) due to evaporation was 13.6 °C. The following equation yields the percentage temperature change due to MCL passage ($\Delta T_{MCL\,(\%)}$) relative to the overall temperature change. The calculated percentage change in temperature due to MCL passage was 71.3 ± 3.7% for the experiment conducted at the surface temperature of 69.7 °C.

$$\Delta T_{MCL(\%)} = (100 \times \frac{\Delta T_1}{\Delta T_2}) \quad (1)$$

The experiment performed at 61.0 °C showed that the temperature rise due to the transition of MCL was 8.9 °C, which constituted 71.2 ±

4.0% of the total temperature change in the sensing zone. Experimental investigation at 53.0 °C also demonstrated a similar result, where the temperature rise associated with the transition of MCL provided 71.0 ± 5.4% of the total temperature rise of 9.3 °C due to the droplet's evaporation. Combinedly, these results show that the passage of the three-phase contact region of an evaporating droplet contributes more than 70% of the overall temperature change during the evaporation process. These results are in excellent agreement with a recent work where Wang et al. used a frequency domain thermo-reflectance method to measure the temperature profile underneath a static evaporating meniscus and found a normalized cumulative heat transfer of 71% occurred within 1 μm of the meniscus edge [55].

The obtained data can further be utilized to quantify the relationship between MCL movement and local vertical heat flux at the surface, i.e., away from the top surface. Figs. 9-11 show the normalized change in local vertical heat fluxes from resistance heater to evaporating droplet for the experiments performed at 69.7 °C, 61.0 °C, and 53.0 °C, where these vertical heat fluxes were calculated from the temperature gradients between resistance heater and RTDs having a vertical separation of 1.2 μm. In these experiments, the local heat flux has a maximum value immediately after dosing, as this is the region where the MCL of the droplet acts as an advancing interface and causes a more significant temperature change due to the deformation of the thermal boundary layer between the dosed water droplet and heated polyimide surface. As shown in Fig. 9, the calculated heat flux for advancing MCL is, on average, 1.21 times the heat flux of receding movement of MCL near the end of the evaporation process. Details on the calculation of the normalized vertical heat flux are given in the Supplementary Materials.

From Fig. 10, the average heat flux value for advancing MCL is 1.40 times the receding MCL. These results also indicate that the heat flux of the receding MCL due to evaporation depends on the MCL's speed as expected. To illustrate, the experiment performed at 69.7 °C enabled, on average, 6.15 times higher heat flux than the initial dry state with an MCL speed of 0.95 mm/s. In contrast, the experiment performed at a lower surface temperature of 61.0 °C facilitated a lower MCL speed of 0.51 mm/s for receding movement, which enabled 5.13 times higher heat flux than the initial dry state.

The heat flux distribution presented in Fig. 9 also shows the advancing and receding MCL passage enables 1.43- and 1.18-times higher heat fluxes, respectively, compared to the heat fluxes produced by the liquid bulk region of the droplet. As summarized in Table 2, the evaporation studies at 61.0 °C and 53.0 °C shown in Figs. 10-11 also exhibit a similar finding, where advancing and receding MCL generated higher heat fluxes than the average heat flux caused by the liquid bulk. These results combinedly support the ideas that the MCL region facilitates the most significant heat transfer for droplet evaporation, the MCL passage produces the maximum local heat fluxes, and that local heat transfer at the MCL is greater for faster-moving MCLs.

Because the micro-device provides measurements of surface temperature distribution with microscale precision, it is also possible to extract the lateral heat flux values at different times during the passage of the MCL. Fig. 12(a) and 13(a) represent the local temperature distribution underneath the evaporating meniscus at various spatial coordinates for experiments performed at 69.7 °C and 61.0 °C. Each of the twelve functioning RTDs employed for these experiments denotes a specific spatial coordinate in the sensing zone of the micro-device. RTD-14L at the leftmost of the sensed region is assigned a relative coordinate of 0 mm, and the remaining RTDs up to RTD-12R correspond to the other positive relative coordinates shown in Figs. 12 and 13. These figures then give the temperature distribution underneath the evaporating droplet at four different times near the end of the evaporation process when the MCL is receding, where coordinates up to 0.64 mm correspond to the wall temperatures underneath the liquid bulk. The axial coordinate 0.84 mm indicates a steep rise in wall temperature caused by the passage of the MCL, which is manifested as an increase in temperature with time.

Fig. 12(b) and 13(b) demonstrate the lateral heat flux distributions calculated from the measured temperatures at various coordinates given in Fig. 12(a) and 13(a). Details on the calculation of the lateral heat flux are in the Supplementary Materials. According to the absolute capacitance change data shown in Figs. 6 and 7, 136.29 s and 165.07 s denote the passage of the MCL from RTD-1R, which has a spatial coordinate of 0.84 mm. Since the MCL passage precedes the actual change in local surface temperature, the times shown in Figs. 12-13 are chosen to portray the associated thermal response. The coordinate 0.84 mm demonstrates both experiments' maximum heat flux values, indicating

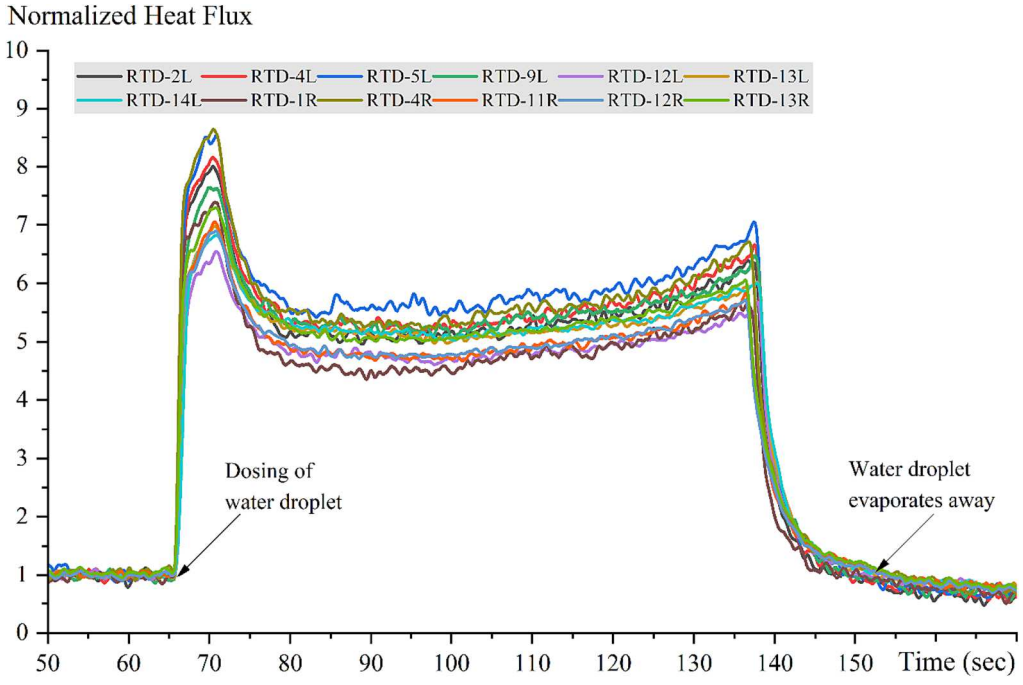

Fig. 9. Normalized heat flux changes with time for an evaporating droplet on a heated polyimide surface at 69.7 °C.

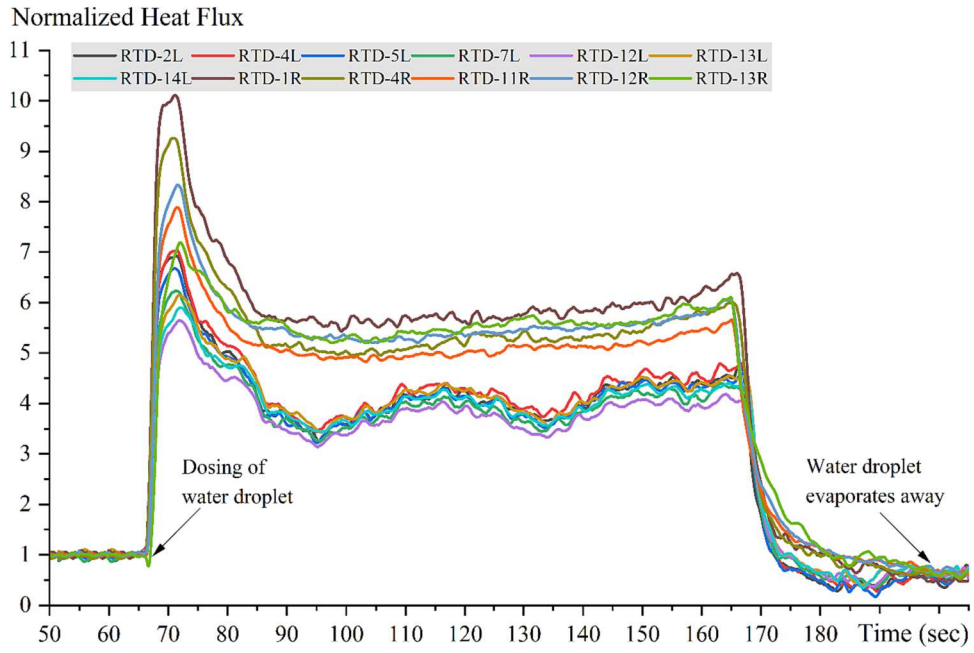

Fig. 10. Normalized heat flux changes with time for an evaporating droplet on a heated polyimide surface at 61.0 °C.

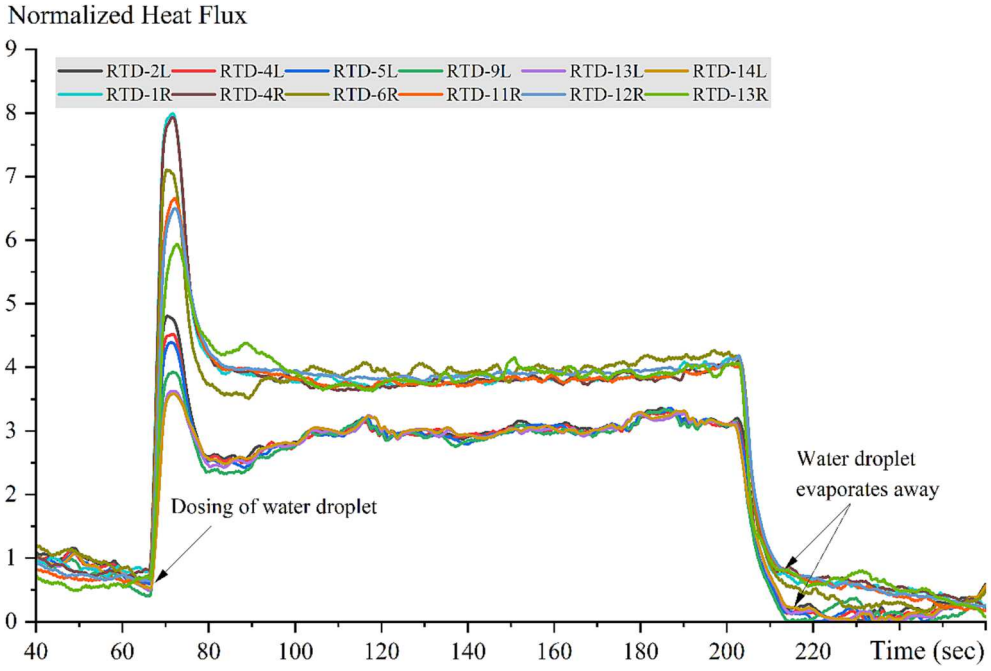

Fig. 11. Normalized heat flux changes with time for an evaporating droplet on a heated polyimide surface at 53.0 °C.

Table 2
Summary of heat flux values caused by advancing MCL, receding MCL, and liquid bulk.

Surface temperature	Avg. heat flux caused by advancing MCL (x initial dry state)	Avg. heat flux caused by receding MCL (x initial dry state)	Avg. heat flux caused by liquid bulk (x initial dry state)
69.7 °C	7.45	6.15	5.22
61.0 °C	7.17	5.13	4.59
53.0 °C	5.50	3.59	3.42

the MCL passage from the sensor region. These results indicate that the lateral heat flux also depends on the MCL's speed. The average heat flux associated with the MCL's passage is 2132 W/m^2 for the experiment conducted at a surface temperature of 69.7 °C, which facilitates a receding MCL speed of 0.95 mm/s. As shown in Fig. 13(b), the investigation conducted at a surface temperature of 61.0 °C with the MCL speed of 0.51 mm/s provides a much lower average heat flux of 828 W/m^2, corresponding to the passage of the slower MCL.

In terms of macroscopic temperature response over the course of the experiment, our results are qualitatively comparable to those of Chen et al. [56] and David et al. [57] despite differences in working fluid, interfacing surface, and experimental approach. They likewise reported

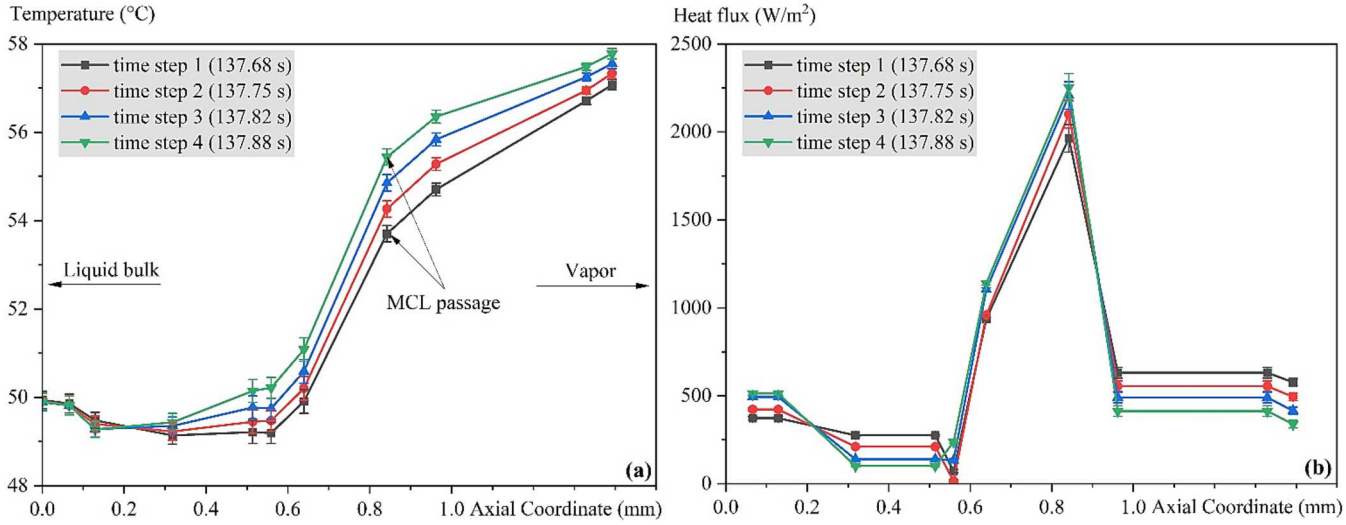

Fig. 12. (a) Local temperature distribution, (b) distribution of lateral heat flux for a receding MCL at surface temperature of 69.7 °C.

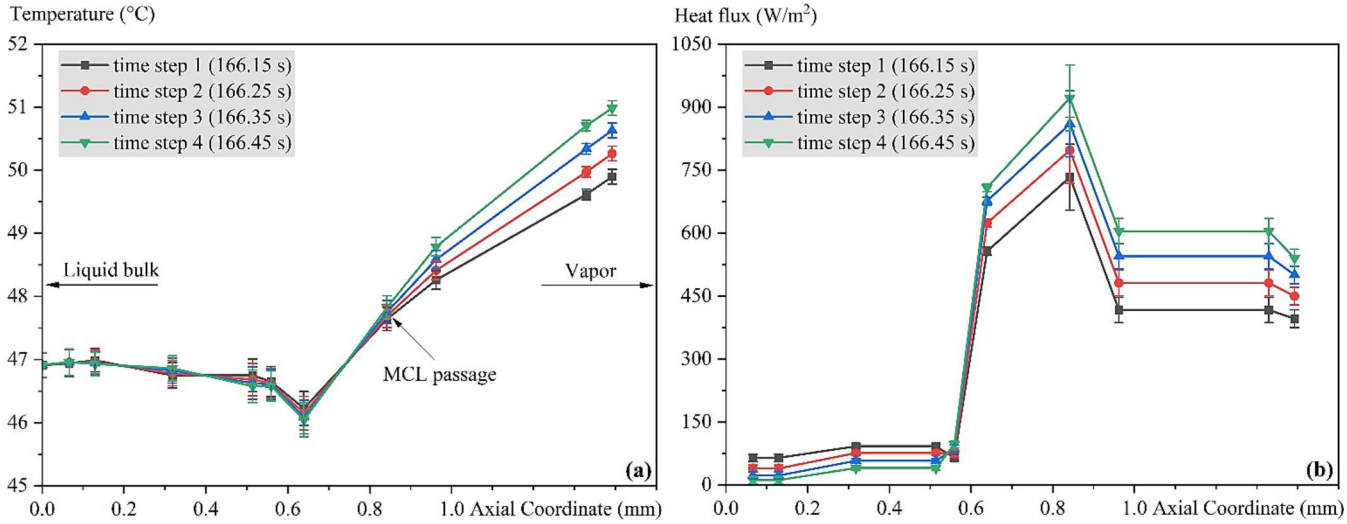

Fig. 13. (a) Local temperature distribution, (b) distribution of lateral heat flux for a receding MCL at surface temperature of 61.0 °C.

a sharp decrease upon droplet deposition, followed by a gradual increase in temperature and another sharp change in temperature near the end of the evaporation process. Microscopically, the closest work to ours may be the IR-based investigations of Ibrahem et al. [18] which utilized HFE7100 as the working fluid. While operating on microscopic RTDs rather than IR imaging analysis, our device likewise allows us to know the lateral temperature distribution across the contact line with microscopic resolution. Our results in Fig. 12(a) and 13(a) for lateral temperature distribution at two different surface temperatures depict a decrease in temperature occurring due to evaporation at the three-phase line before a notable increase in temperature as one moves from inside the liquid region to the vapor region without. Also, an increase in surface temperature/heat flux results in a deeper temperature dip. Similar observations were reported in Ibrahem et al. [18]. However, in that work the position of the contact line was defined as coinciding with the location of the local temperature minimum. For our work, we do not rely on such a definition and instead have independent tracking the location of the contact line via the IDE sensors. This is an important distinction and a major part of the novelty and utility of our work. As shown in Fig. 12(a) and 13(a), we note that the minimum temperature occurs just *inside* the contact line on the liquid side but still within 200–300 μm of the contact line location as measured by the IDEs. For comparison, our lateral tracking resolution for the contact line is estimated to be ~ 100 μm and the entire region of contact line influence on temperature approximately 600 μm.

A similar discussion can be had in regards to heat flux, which in our case is determined via the RTD-measured temperature distributions and also benefits from independent contact line sensing via the IDEs in a similar manner to above. Raj et al. [22] conducted numerical modeling to study the heat flux associated with the movement of the contact line of an evaporating droplet. They found that the heat flux initially increased to a maximum value at the moving contact line region and subsequently decreased due to the growing thickness of the liquid film in the bulk region. Ibrahem et al. [18] demonstrated that the defined contact line region exhibited the highest heat flux, attributed to its high evaporation rate. Here again, our current study aligns well with these previous works as depicted in Fig. 12(b) and 13(b), which gives confidence as to its results. Similar to the temperature distribution discussion, however, our direct contact line tracking shows that the highest heat flux does indeed coincide with the MCL's passage for both surface temperatures without the need to infer such a conclusion. This supports existing theoretical and numerical studies that predict such phenomenon due to the strong gradients in the region. Quantitatively, Ibrahem et al. [18] found that the local heat fluxes near the contact line were

5.4–6.5 times higher than the mean heat flux. Our work puts this ratio at about 5.50–7.45 for the faster-moving advancing MCL and 3.59–6.15 for the slower receding MCL cases, respectively. Additionally, Wang et al. [55] employed a frequency domain thermo-reflectance method to measure the temperature profile beneath an evaporating meniscus. They found that approximately 71% of the normalized cumulative heat transfer occurred within 1 μm of the meniscus edge. This finding is in excellent agreement with our current work, as Figs. 6-8 demonstrate that the passage of the three-phase contact region of an evaporating droplet contributes to over 70% of the overall temperature change during the evaporation process.

4. Conclusions

Water droplet evaporation on a heated polyimide surface was investigated at various temperatures to determine the underlying physics behind the phase-change heat transfer and mechanistic interdependence between the three-phase moving contact line and temperature distribution underneath the evaporating droplet. A microfabricated composite device comprising phase-interface sensing capacitance sensors and temperature sensing RTDs was employed to keep track of the MCL and measure temperature distribution underneath the evaporating meniscus. Experimental investigations were performed to determine the impact of MCL's speed and direction of motion on the overall evaporative heat transfer, where the results showed that the MCL precedes the actual change in local surface temperature and the timing differences between these events depends on the speed of the MCL. The following conclusions can also be drawn from the experimental investigations:

- The passage of the three-phase contact region of an evaporating droplet contributes more than 70% of the overall temperature change during the evaporation process.
- The time lag between MCL passage and associated thermal response depends on the speed of MCL. The evaporation study at 69.7 °C showed a time lag of 0.81 s with an MCL speed of 0.95 mm/s, while the experiment at 61.0 °C and 53.0 °C enabled extended time lag of 1.27 s and 1.43 s with slower MCL speed of 0.51 mm/s and 0.47 mm/s, respectively.
- Advancing MCL of an evaporating droplet due to dosing exhibited a more significant temperature change than the temperature change associated with a receding MCL due to evaporation. The magnitude of temperature difference caused by advancing and receding movement depends on the speed of the MCL; the higher the MCL's speed, the greater the temperature difference.
- The average heat flux value for advancing MCL was 5.50–7.45 times the initial dry state and 1.21–1.53 times higher than the receding MCL.
- The MCL region facilitated the most significant heat transfer for droplet evaporation. The advancing and receding MCL passage enabled 1.43–1.61 times and 1.05–1.18 times higher heat fluxes, respectively, compared to the heat fluxes produced by the liquid bulk region of the droplet.
- Due to the significant differences in wall temperature underneath the liquid bulk and MCL regions, the maximum local heat flux values occurred at the three-phase contact line.
- The lateral heat flux also depends on the MCL's speed and surface temperature. The MCL's speed of 0.95 mm/s provided 2.57 times higher heat flux in the MCL region compared to the experiment that facilitated an MCL's speed of 0.51 mm/s.

In the future, this composite micro-device is envisioned to investigate evaporating meniscus of nonaqueous liquids, of liquid-surface combinations with varying controlled wettability, and to study the dynamics of heat transfer and phase-interface behavior involved in nucleate boiling processes.

CRediT authorship contribution statement

Md Tanbin Hasan Mondal: Investigation, Writing – original draft. **Rifat-E-Nur Hossain:** Investigation, Writing – original draft. **Ronald Martin:** Investigation, Writing – original draft. **Arden L. Moore:** Conceptualization, Writing – review & editing.

Declaration of Competing Interest

The authors declare that they have no known competing financial interests or personal relationships that could have appeared to influence the work reported in this paper.

Data availability

Data will be made available on request.

Acknowledgements

This material is based upon work supported by the National Science Foundation under Grant Number 1846165.

Appendix A. Supplementary data

Supplementary data to this article can be found online at https://doi.org/10.1016/j.applthermaleng.2023.121477.

References

[1] M.M. Nahar, et al., "Review article: Microscale evaporative cooling technologies for high heat flux microelectronics devices: Background and recent advances,", Appl. Therm. Eng. 194 (2021).
[2] D. Zang, S. Tarafdar, Y.Y. Tarasevich, M. Dutta Choudhury, T. Dutta, Evaporation of a Droplet: From physics to applications, Phys. Rep. 804 (2019) 1–56.
[3] M.J. Gibbons, P. Di Marco, A.J. Robinson, Local heat transfer to an evaporating superhydrophobic droplet, Int. J. Heat Mass Transf. 121 (2018) 641–652.
[4] S.Y. Misyura, Evaporation of a sessile water drop and a drop of aqueous salt solution, Sci. Rep. 7 (1) (2017) 1–11.
[5] S. Semenov, V.M. Starov, M.G. Velarde, R.G. Rubio, Droplets evaporation: Problems and solutions, Eur. Phys. J. Spec. Top. 197 (1) (2011) 265–278.
[6] O.E. Ruiz, W.Z. Black, Evaporation of water droplets placed on a heated horizontal surface, J. Heat Transfer 124 (5) (2002) 854–863.
[7] R.K. Mandel, D.G. Bae, M.M. Ohadi, "Embedded two-phase cooling of high flux electronics via press-fit and bonded FEEDS coolers,", J. Electron. Packag. 140 (3) (2018).
[8] S.K. Wilson, H.M. D'Ambrosio, Evaporation of sessile droplets, Annu. Rev. Fluid Mech. 55 (2023) 481–509.
[9] Z. Zheng, L. Zhou, X. Du, Y. Yang, Numerical investigation on conjugate heat transfer of evaporating thin film in a sessile droplet, Int. J. Heat Mass Transf. 101 (2016) 10–19.
[10] E. Lakew, A. Sarchami, G. Giustini, H. Kim, K. Bellur, "Thin film evaporation modeling of the liquid microlayer region in a dewetting water bubble,", Fluids 8 (4) (2023).
[11] K. Chen, R.N. Xu, P.X. Jiang, Evaporation enhancement of microscale droplet impact on micro/nanostructured surfaces, Langmuir 36 (41) (2020) 12230–12236.
[12] A.-M. Cazabat, G. Guéna, Evaporation of macroscopic sessile droplets, Soft Matter 6 (12) (2010) 2591–2612.
[13] A.L. Karchevsky, I.V. Marchuk, O.A. Kabov, Calculation of the heat flux near the liquid–gas–solid contact line, App. Math. Model. 40 (2) (2016) 1029–1037.
[14] P.A. Raghupathi, S.G. Kandlikar, Contact line region heat transfer mechanisms for an evaporating interface, Int. J. Heat Mass Transf. 95 (2016) 296–306.
[15] J.L. Plawsky, et al., Nano-and microstructures for thin-film evaporation-A review, Nanoscale Microscale Thermophys. Eng. 18 (3) (2014) 251–269.
[16] C.P. Migliaccio, H.K. Dhavaleswarapu, S.V. Garimella, Temperature measurements near the contact line of an evaporating meniscus V-groove, Int. J. Heat Mass Transf. 54 (7–8) (2011) 1520–1526.
[17] H.K. Dhavaleswarapu, S.V. Garimella, J.Y. Murthy, Microscale temperature measurements near the triple line of an evaporating thin liquid film, J. Heat Transfer 131 (6) (2009) 1–7.
[18] K. Ibrahem, M.F. Abd Rabbo, T. Gambaryan-Roisman, P. Stephan, Experimental investigation of evaporative heat transfer characteristics at the 3-phase contact line, Exp. Therm Fluid Sci. 34 (8) (2010) 1036–1041.
[19] S.S. Panchamgam, A. Chatterjee, J.L. Plawsky, P.C. Wayner, Comprehensive experimental and theoretical study of fluid flow and heat transfer in a microscopic evaporating meniscus in a miniature heat exchanger, Int. J. Heat Mass Transf. 51 (21–22) (2008) 5368–5379.

[20] P. Stephan, C.A. Busse, Analysis of the heat transfer coefficient of grooved heat pipe evaporator walls, Int. J. Heat Mass Transf. 35 (1992) 383–391.
[21] X. Xu, V.P. Carey, Film evaporation from a micro-grooved surface—an approximate heat transfer model and its comparison with experimental data, J. Thermophys Heat Transfer 4 (4) (1990) 512–520.
[22] R. Raj, C. Kunkelmann, P. Stephan, J. Plawsky, J. Kim, Contact line behavior for a highly wetting fluid under superheated conditions, Int. J. Heat Mass Transf. 55 (9–10) (2012) 2664–2675.
[23] B. Sobac, D. Brutin, Triple-line behavior and wettability controlled by nanocoated substrates: Influence on sessile drop evaporation, Langmuir 27 (24) (2011) 14999–15007.
[24] J.G. Myers, V.K. Yerramilli, S.W. Hussey, G.F. Yee, J. Kim, Time and space resolved wall temperature and heat flux measurements during nucleate boiling with constant heat flux boundary conditions, Int. J. Heat Mass Transf. 48 (12) (2005) 2429–2442.
[25] C. Kunkelmann, K. Ibrahem, N. Schweizer, S. Herbert, P. Stephan, T. Gambaryan-Roisman, The effect of three-phase contact line speed on local evaporative heat transfer: Experimental and numerical investigations, Int. J. Heat Mass Transf. 55 (7–8) (2012) 1896–1904.
[26] E.F. Crafton, W.Z. Black, Heat transfer and evaporation rates of small liquid droplets on heated horizontal surfaces, Int. J. Heat Mass Transf. 47 (6–7) (2004) 1187–1200.
[27] C. Sodtke, V.S. Ajaev, P. Stephan, Dynamics of volatile liquid droplets on heated surfaces: Theory versus experiment, J. Fluid Mech. 610 (2008) 343–362.
[28] T.H. Kim, E. Kommer, S. Dessiatoun, J. Kim, Measurement of two-phase flow and heat transfer parameters using infrared thermometry, Int. J. Multiph. Flow 40 (2012) 56–67.
[29] S.W. Paik, K.D. Kihm, S.P. Lee, D.M. Pratt, Spatially and temporally resolved temperature measurements for slow evaporating sessile drops heated by a microfabricated heater array, J. Heat Transfer 129 (8) (2007) 966–976.
[30] M. Buchholz, T. Lüttich, H. Auracher, W. Marquardt, Experimental investigation of local processes in pool boiling along the entire boiling curve, Int. J. Heat Fluid Flow 25 (2) (2004) 243–261.
[31] M. Buchholz, H. Auracher, T. Lüttich, W. Marquardt, A study of local heat transfer mechanisms along the entire boiling curve by means of microsensors, Int. J. Therm. Sci. 45 (3) (2006) 269–283.
[32] H. Auracher, W. Marquardt, Heat transfer characteristics and mechanisms along entire boiling curves under steady-state and transient conditions, Int. J. Heat Fluid Flow 25 (2) (2004) 223–242.
[33] R. Raj, J. Kim, J. McQuillen, Pool boiling heat transfer on the international space station: Experimental results and model verification, J. Heat Transfer 134 (10) (2012) 1–14.
[34] R. Raj, J. Kim, J. McQuillen, On the scaling of pool boiling heat flux with gravity and heater size, J. Heat Transfer 134 (1) (2012) 1–13.
[35] J. Jung, S.J. Kim, J. Kim, Observations of the critical heat flux process during pool boiling of FC-72, J. Heat Transfer 136 (4) (2014).
[36] S. Bae, M. Kim, J. Kim, Improved technique to measure timeand space-resolved heat transfer under single bubbles during saturated pool boiling of fc-72, Exp. Heat Transf. 12 (3) (1999) 265–278.
[37] Y. Fukatani, D. Orejon, Y. Kita, Y. Takata, J. Kim, K. Sefiane, Effect of ambient temperature and relative humidity on interfacial temperature during early stages of drop evaporation, Phys. Rev. E 93 (4) (2016) 1–16.
[38] L. Bogdanic, H. Auracher, F. Ziegler, Two-phase structure above hot surfaces in jet impingement boiling, Heat Mass Transf. und Stoffuebertragung 45 (7) (2009) 1019–1028.
[39] H. Robidou, H. Auracher, P. Gardin, M. Lebouché, Controlled cooling of a hot plate with a water jet, Exp. Therm Fluid Sci. 26 (2–4) (2002) 123–129.
[40] H. Auracher, W. Marquardt, Experimental studies of boiling mechanisms in all boiling regimes under steady-state and trnsient conditions, Int. J. Therm. Sci. 41 (7) (2002) 586–598.
[41] Y.M. Qiao, S. Chandra, Experiments on adding a surfactant to water drops boiling on a hot surface, Proc. R. Soc. A Math. Phys. Eng. Sci. 453 (1959) (1997) 673–689.
[42] S. Chandra, C.T. Avedisian, Evaporation and combustion of levitated arrays of two, three and five droplets At a hot surface, Proc. R. Soc. London, Ser. A Math. Phys. Sci. 418 (1855) (1988) 365–382.
[43] S. Chandra, C.T. Avedisian, On the collision of a droplet with a solid surface, Proc. R. Soc. A Math. Phys. Eng. Sci. 432 (1884) (1991) 13–41.
[44] J.D. Bernardin, I. Mudawar, C.B. Walsh, E.I. Franses, Contact angle temperature dependence for water droplets on practical aluminum surfaces, Int. J. Heat Mass Transf. 40 (5) (1997) 1017–1033.
[45] J.D. Bernardin, C.J. Stebbins, I. Mudawar, Effects of surface roughness on water droplet impact history and heat transfer regimes, Int. J. Heat Mass Transf. 40 (1) (1996) 73–88.
[46] C. Elbuken, T. Glawdel, D. Chan, C.L. Ren, Detection of microdroplet size and speed using capacitive sensors, Sens. Actuators, A 171 (2) (2011) 55–62.
[47] J.Z. Chen, A.A. Darhuber, S.M. Troian, S. Wagner, Capacitive sensing of droplets for microfluidic devices based on thermocapillary actuation, Lab Chip 4 (5) (2004) 473–480.
[48] M.T.H. Mondal, T. Desai, R.-E.-N. Hossain, A.L. Moore, Microscale tracking of unconstrained moving multiphase contact lines via a capacitance sensor array, Sens. Actuators, A 331 (2021) 113046.
[49] P. Kubra Isgor, M. Marcali, M. Keser, C. Elbuken, Microfluidic droplet content detection using integrated capacitive sensors, Sensors Actuators, B Chem. 210 (2015) 669–675.
[50] S.A. Putnam, et al., Microdroplet evaporation on superheated surfaces, Int. J. Heat Mass Transf. 55 (21–22) (2012) 5793–5807.
[51] J. Kim, J. Kim, Y. Shin, Y. Yoon, A study on the fabrication of an RTD (Resistance Temperature Detector) by using Pt thin film, Korean J. Chem. Eng. 18 (1) (2001) 61–66.
[52] Y. Wang, C. Zhang, J. Li, G. Ding, L. Duan, Fabrication and characterization of ITO thin film resistance temperature detector, Vacuum 140 (2017) 121–125.
[53] M.T.H. Mondal, R.-E.-N. Hossain, R. Martin, A.L. Moore, Speed and location tracking of moving multiphase interfaces via a capacitance microsensor array during droplet evaporation, Micro Nano Eng. 17 (2022) 100168.
[54] X.Y. Zhao, H.J. Liu, Review of polymer materials with low dielectric constant, Polym. Int. 59 (5) (2010) 597–606.
[55] X. Wang, S.A. Ghaffarizadeh, X. He, A.J.H. McGaughey, J.A. Malen, Ultrahigh evaporative heat transfer measured locally in submicron water films, Sci. Rep. 12 (1) (2022) 22353.
[56] T. Chen "Heat transfer to wetting and non-wetting liquid droplets deposited onto a heated microgroove surface," *Proc. 15th Intersoc. Conf. Therm. Thermomechanical Phenom. Electron. Syst. ITherm 2016* 987 993.
[57] S. David, K. Sefiane, L. Tadrist, Experimental investigation of the effect of thermal properties of the substrate in the wetting and evaporation of sessile drops, Colloids Surfaces A Physicochem. Eng. Asp. 298 (1–2) (2007) 108–114.